Chiro-optical response of a wafer scale metamaterial with ellipsoidal metal nanoparticles

To cite this article before publication: Akanksha Ninawe *et al* 2021 *Nanotechnology* in press https://doi.org/10.1088/1361-6528/abf877

IOP Publishing Journal Title
Journal **XX** (XXXX) XXXXXX https://doi.org/XXXX/XXXX

Chiro-Optical Response of a Wafer Scale Metamaterial with Ellipsoidal Metal Nanoparticles

Akanksha Ninawe[1], Priyanka Suri[2], Zhuolin Xie[2], Xianfan Xu[3*] and Ambarish Ghosh[2,4*]

[1] Department of Electrical Engineering, Indian Institute Technology Delhi, Hauz Khas, New Delhi 110016, India
[2] Centre for Nano Science and Engineering, Indian Institute of Science, Bangalore, India
[3]School of Mechanical Engineering and Birck Nanotechnology Center, Purdue University, West Lafayette, Indiana 47907, USA
[4]Department of Physics, Indian Institute of Science, Bangalore, India

E-mail: xxu@purdue.edu, ambarish@ece.iisc.ernet.in

Received xxxxxx
Accepted for publication xxxxxx
Published xxxxxx

Abstract

We report a large chiro-optical response from a nanostructured film of aperiodic dielectric helices decorated with ellipsoidal metal nanoparticles. The influence of the inherent fabrication variation on the chiro-optical response of the wafer-scalable nanostructured film is investigated using a computational model which closely mimics the material system. From the computational approach, we found that the chiro-optical signal is strongly dependent on the ellipticities of the metal nanoparticles and the developed computational model can account for all the variations caused by the fabrication process. We report the experimentally realized dissymmetry factor ~1.6, which is the largest reported for wafer scalable chiro-plasmonic samples till now. The calculations incorporate strong multipolar contributions of the plasmonic interactions to the chiro-optical response from the tightly confined ellipsoidal nanoparticles, improving upon the previous studies carried in the coupled dipole approximation regime. Our analyses confirm the large chiro-optical response in these films developed by a scalable and simple fabrication technique, indicating their applicability pertaining to manipulation of optical polarization, enantiomer selective identification and enhanced sensing and detection of chiral molecules.

Supplementary material for this article is available

Keywords: chiral plasmonics, helical nanostructures, ellipsoidal nanoparticles, dissymmetry factor, multipolar interactions, finite element method, enantiomer detection

1. Introduction

Chiral plasmonics is an intriguing field of research with exemplary designs of chiro-optical structural configurations with diverse applications in nanophotonics such as negative refractive index [1], [2], chiral biomolecular detection [3], [4], chiral magnetic materials [5], enantiomer selection [6]–[11], broadband circular polarizers [12]–[14], chiral optical tweezers [15], [16] and nanomedicine [17]. Several recent and interesting advances towards enhancing the inherently weak optical chirality of naturally chiral materials and improving chiral light-matter interactions include reports on investigation of planar chiral metamaterials [18]–[21], fabrication of chiral magnetic nanoparticles and gels [22], measurement of enantioselective optical forces between a chiral plasmonic probe and a bull's-eye grating substrate [23], chiral photothermal plasmonic effects in metamaterial absorbers [24], multichirality evolution step synthesis method

for enhanced chiro-optical response [25], anisotropic material modulated chiro-optical response [26], magnetic field assisted real-time chirality modulation [27], chiral fluorescence from silver nanoclusters [28] and 3D chiral nanostructures [11], [29]–[31]. Recently, the scope of artificial chiral metametarials has expanded from nanoscale structures to bulk chiral mechanical metamaterials with successful industrial applications [32], [33]. The field of chiral electromagnetics and metamaterials is quite mature, and therefore, a vast literature is dedicated towards versatile fabrication techniques of chiral nanostructures and metamaterials [34], [35]. Researchers have incorporated different fabrication approaches to induce chirality into nanostructures such as fabrication of inherently chiral nanomaterials and metamaterials [12], [36]–[38], template dependent chiral nanostructures [39]–[45] and fabrication of chiral nano-assemblies from achiral components [46]–[48]. The top-down fabrication approaches such as laser direct write or electron beam lithography are known to offer precise control of the structural parameters. These techniques also have their own limitations, for instance, the femtosecond laser direct write technique cannot be employed to develop nanostructures for visible or near-infrared regime due to the resolution limit [12], [49]. The wafer-scalabilty of the fabricated structures in the case of focussed ion beam or electron beam deposition techniques is largely limited due to the extremely low throughput of the deposited material [50]. Further, the complexity of the lithography techniques increases in the case of stacked metamaterials [4], [48], [51] or nanostructures fabricated using on-edge lithography [52] which demands alignment precision. The bottom-up fabrication strategies for the synthesis of chiral nanostructures are predominantly based on directed assembly of nanoparticles into larger complex structures for attaining the desired chiral signatures based on vapor deposition schemes, such as GLAD (Glancing Angle Deposition) [53], [54]. This fabrication strategy is refractive index tunable [55], cost effective, highly wafer scalable, and applicable to both plasmonic [56], [57], as well as dielectric [58]–[61] chiral metamaterials. However, in comparison to the top-down techniques, precise control of the self-assembled nanostructures is generally not feasible due to the intrinsic randomness of the assembly and subsequent shadowing processes. Naturally, the chiro-optical signal of the self-assembled nanostructures with large geometric variations have an inherent tuning capability and the dimensional parameters can be modulated by the helical template and the assembled chiral particles. To computationally investigate the influence of large structural variabilities on the chiro-optical signal in these highly scalable wafers such as self–assembled nanoparticles arranged on a helical template, a computational model based on the conventional finite element or finite difference time domain (FDTD) methods requires large computational resources. Some previous works [56], [62] have based the analytical investigation on semi-analytical method based on coupled dipole approximation (CDA) model [63]–[65] in which the chirally arranged NPs are considered as interacting dipoles where the center to center distance between particles (r) is more than three times the particle radius (a), i.e., $r/a>3$. While the CDA provides the preliminary investigation of the influence of structural parameters on the chiro-optical signal, this model is far from the actual arrangement of particles in the experimental system which are within $r/a<3$ regime and the higher order multipolar contributions due to electromagnetic interactions are significantly predominant as established in theoretical [66]–[70] and experimental [71], [72] works on 1-D and 2-D nanoparticle arrays. Further, Nair et al [73]have investigated the influence of interparticle separation on the chiro-optical signal in $r/a<3$ regime and have found that the CDA remains valid until around $r/a \approx 2.3$ and the multipolar effects includes significant redshift and spectral broadening of the chiro-optical response in close agreement with the theory proposed in [66], [67]. In this study, we develop a computational model to investigate the chiro-optical signature of an assembly of three-dimensional chiral NPs arranged on a dielectric helical template and correlate the computationally evaluated enhanced chiro-optical signal with the actual experimental system. The model considers predominantly ellipsoidal NPs held in tighter confinement and thus the effect of multipolar contributions on the chiro-optical response is significant and close to the experimental observations. Further, the influence of variations in the dimensional parameters of the helical template are also numerically investigated.

2. Methods

2.1 Numerical simulations: FEM-COMSOL.

We used a finite element method-based solver COMSOL Multiphysics to numerically evaluate the performance of the chiral nanostructures. The full field formulation with periodic boundary condition was adopted to realize an infinite periodic array of the helices in x-y plane with light incident from z-direction using input excitation port. The incident circularly polarized beam is propagating parallel to the helix axis. The port is placed at $\lambda/2$ distance away from the nanostructure to avoid near field effects. For studying the effect of a standalone single strand of helix, we used a PML of thickness 150 nm and order one surrounding the model geometry in x-y plane and away from the nanostructure by $\lambda/2$ to avoid near-field effects. A dynamic tetrahedral mesh of size 3.2 nm is used for the particles and maximum size of $\lambda/6$ is used for rest of the geometry. The wavelength dependent complex dielectric function of silver is taken from [74]. Wavelength sweep is used to scan in the range from 400 to 800 nm.

2.2 Fabrication

In the first step of fabrication, SiO_2 rods are grown over piranha cleaned glass slides using the conventional GLAD technique [56], [58], [59], [62], [73] at an extreme tilt of 84 degrees to the incident vapors. With the substrate continuously rotating, rods of length about 200 nm are grown, without any seed layer. The average distance between the rods is 50 nm. Once the desired length is attained, helices are grown on them in the same run by rotating the substrate at 2 degree/step. The number of steps is decided by the pitch and turns required in a helix. Deposition rate for SiO_2 for both rods and helices is maintained between 0.6-1 A/s. The handedness of the helices is decided by the rotation (clockwise or anticlockwise) of the substrate with respect to the flux. Standing helices with pitch of about 280 nm and 2 turn are thence fabricated with a very high throughput. The rods are only fabricated to give length enough to the nanostructure to be distinguishable in microscope and do not contribute to chirality.

The next step of fabrication is coating the helices with silver nanoparticles. The tilt of the substrate is reduced to 10º with the incoming metal vapors and deposition of a silver thin film of thickness 10 nm, is done using E-beam evaporation. For E-beam deposition of silver, we take the previously fabricated standing helices substrate and place it parallel to the material crucible (0º with the incoming flux). Simple line of sight deposition was not effective in ensuring complete coverage of the helices with silver till the end and therefore a tilt angle of 10º with respect to the incoming flux is provided to the sample to ensure that the metal vapors go along the chiral geometry providing complete coverage till the bottom. These samples are then annealed @260 ºC for 20 minutes to decorate the helices with silver nanoparticles. Deposition rate is maintained between 0.1-0.2 A/s. Silver annealing at different temperatures and as a function of underlying substrate has been explored by many groups from an application perspective [56], [75], [76]. The average size of these particles is between 50-100 nm and an average separation between 20-40 nm.The large area wafer-scale metamaterial films in our study have sample sizes of at least ~ 1 cm by 1.5 cm. The schematic describing the complete technological process is shown in Fig. 1.

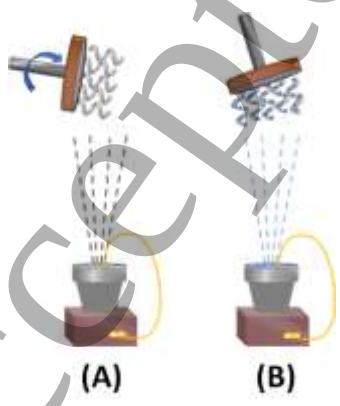

Figure 1. Fabrication technology. (A) Fabrication of SiO_2 helices using GLAD at 84º tilt of substrate with incoming vapor flux. (B) Coating of standing helices with silver at 10º tilt with incoming flux.

2.3 Optical Characterization

The wafer-scale films of left and right-handed metal decorated chiral unheated samples were optically characterized by measuring the large chiro-optical response exhibited by the two films. The optical measurements for transmission were performed using a home-built setup. A quartz tungsten-halogen lamp is used as a white light source. The beam from the quartz tungsten halogen white light source passes through an adjustable square aperture which is placed at the focal length of a parabolic mirror to minimize chromatic aberrations. The aperture is adjusted to change the spot size. The spot size used in experiments is ~ 40 µm. The size of the illuminated area on the sample is equal to the size of the beam which is 40 µm. This is followed by a polarizer and a retarder combination (Fresnel Rhomb FR600QM) to transform the transmitted beam into left or right circularly polarized beam. The polarization-controlled light (left or right) is further guided through several optics through an infinity corrected 100x objective with NA 0.8 and WD 3.5 mm to the sample (corresponding to which the cone angle of illumination is 106.26º). Transmitted light from the sample is collected by an infinity corrected 50x objective with NA 0.55 and WD 10.1 mm (corresponding to which the cone angle of collection is 66.73º) and sent to the fiber optic spectrometer. A silver-coated off-axis parabolic mirror of effective focal length (EFL) of 15.2 cm was used to send the collimated transmitted light into the commercial spectrometer (Ocean Optics). For each sample spectrum measurement, reference correction was performed by subtracting an appropriate dark spectrum (captured by blocking ambient light) and dividing by the reference corrected spectrum. The collection objective is mounted on a translational stage. The reference for all measurements is taken in air by adjusting the z-translational motion of the 3–stage piezo on which the sample is mounted. The transmittance signal for LCP/RCP illumination is obtained as

$$T_{LCP(RCP)} = \frac{I_{LCP(RCP)}(\lambda) - I_{dark}(\lambda)}{I_{ref}(\lambda) - I_{dark}(\lambda)} \qquad (1)$$

The light is further guided through several optics and sent to a fiber optic spectrometer (Ocean Optics). The normal alignment of the incident light on the sample is confirmed as only the z-translational motion of the piezo stage is to be changed to maximize the transmitted signal through the sample. The x- and y- positions on the piezo remain the same for one sample location in all measurements when light is focused with and without the sample. The sample is imaged in reflection mode using a 90/10 beam-splitter in the path of light before sending it to the 100x objective. A flip mount mirror when mounted is used to send the transmitted light from the

sample collected by the 50x objective to a CCD camera to read the image of the sample in transmission mode. The flip mount mirror when unmounted guides the collimated light through a parabolic mirror to the spectrometer.

3. Results and Discussion

To investigate and correlate the chiro-optical response of the experimental system with computational analysis, we considered unseeded (without predefined periodic seed layers) aperiodic dielectric silica helices with decorated AgNPs. Figures 2A–B show the side view SEM of the nanostructured thin films grown by glancing angle deposition (GLAD) technique on left and right-handed samples respectively. For the quantification of the asymmetric transmission from the samples for the two states of circularly polarized light, we define a quantity called dissymmetry factor (g), calculated as $g = \frac{\Delta T}{T_{avg}}$, where ΔT is circular differential (CD) transmittance, calculated as $\Delta T = T_{LCP} - T_{RCP}$, where T_{LCP} and T_{RCP} are transmission spectra of the sample under LCP and RCP illumination respectively and T_{avg} is the average transmittance of the sample. Figure 2C and 2D show spectral responses of dissymmetry factor g for both samples measured at four different locations on the samples. It is noted that the chiro-optical response reverses sign with the handedness of the helix which is expected. The experimentally realized dissymmetry factor g ~ 1.6 is thus far the highest reported for a wafer scalable chiro-plasmonic sample. A comparison of the experimentally realized dissymmetry factors for different small area and large-area chiro-plasmonic structures reported in literature is presented in Table 1. The chiro-optical response of the two samples of opposite handedness are sign reversed as expected, however, $|g|$ values are larger for right handed sample as compared with left handed sample, which could possibly be explained by the asymmetric fabrication parameters such as helices thickness which can happen because of fast fluctuations in rate of SiO_2 depositions. The results for estimation of the contribution of linear dichroism (LD), which is the difference in absorption (or transmission) of linearly polarized light with orthogonal polarization planes, on the measurement of chiro-optical responses of the samples is presented in Fig. S1. We estimated the contribution from LD to the measurement of circular dichroism by measuring CD signals from the samples when the substrate is rotated for various rotation angles and incident light normal to the substrate. Figure S1 show the measured CD transmittance as a function of substrate rotation for left (Fig. S1(A)) and right-handed (Fig. S1(B)) samples. It is noted that there is a slight variation in the CD as a function of different rotation angles and it appears that LD might have a small effect on the measurement of CD. Alternatively, it is also possible that the density of helices interacting with light might change with substrate rotation due to the growth of aperiodic helices on the unseeded substrate samples. The GLAD technique works on rotating the substrate kept at an extreme angle with respect to the source of vapor, formed through physical vapor deposition techniques like electron beam or thermal evaporation. The films thus grown on an unseeded substrate show random morphological variations such as silica helices at non-uniform separations, deposition of random residual silver on bare substrate during GLAD, or variations in NP sizes. In wafers which are fabricated with a seeded patterned substrate, the incoming flux at extreme angle sees and sits on the pattern only, forming a periodically arranged uniform substrate, their widths corresponding to the widths of the seeds. With an unseeded substrate as ours, however, there is no control on the arrangement of the incoming flux and the widths of these columns and helices grown. This has been explained in detail in [77]. The porosity variations so caused across the samples result in different degree with which the Ag vapor goes lower within the helices. The sheer intrinsic nature of the annealing process also causes randomness of size of islands [75], [78], further adding to the morphological variations and to the angle dependence of CD. Despite the variabilities occurring due to the inherent nature of the fabrication process, the averaged chiro-optical response of the material noted from the experiments remained almost uniform across the wafer.

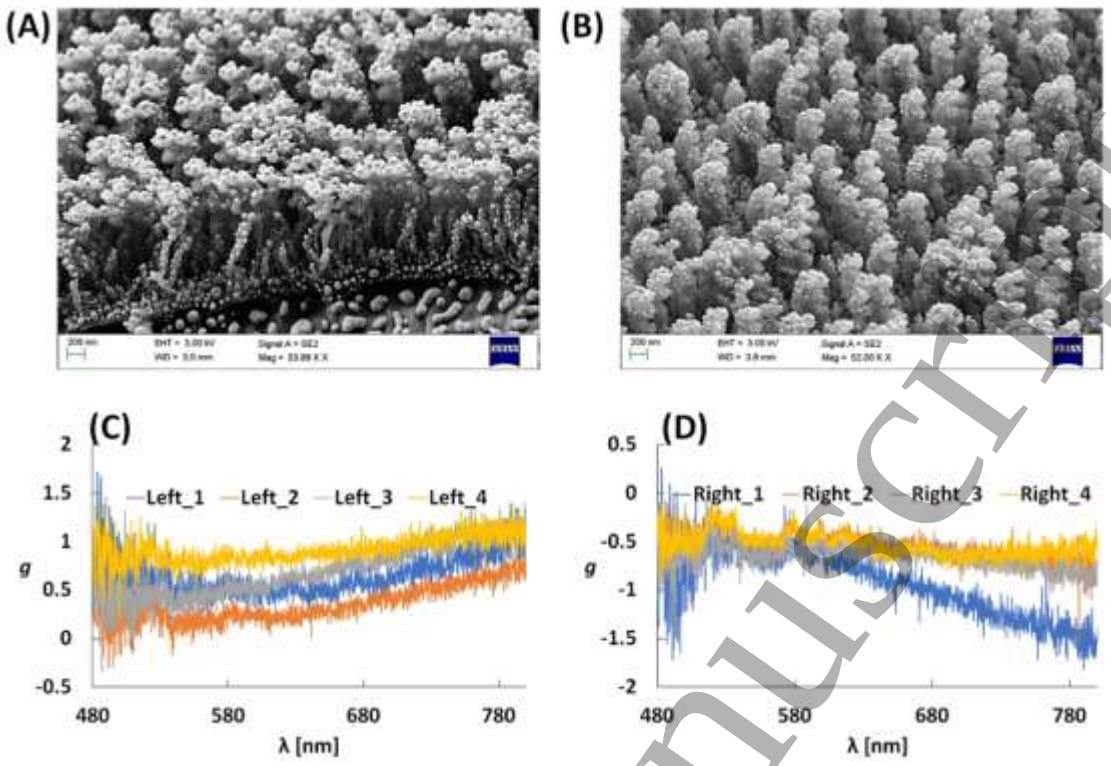

Figure 2. Scanning electron micrograph of (A) left-handed and (B) right-handed chiral samples. Spectral response of dissymmetry factor *g* for (C) left-handed and (D) right-handed chiral samples measured at four different locations.

Table 1. Comparison of the experimentally realized dissymmetry factors for different small area and large-area chiro-plasmonic structures reported in literature.

Ref no.	Fabrication approach	Type of nanostructure	Experimentally realized dissymmetry factor/anisotropy factor values
[59]	Bottom-up approach, GLAD (large area materials)	Helical core-shell nanostructures	Transmittance spectra not given
[79]	Electron beam induced deposition (EBID) (small area materials)	Silver coated helices	0.45 (single silver helix) at 550 nm
[80]	Focused ion beam with gradient milling approach (small area materials)	Ramp shaped gold nanostructures with azimuthally gradient depth	1.13 and 0.8 for LH and RH structures respectively at 678 nm
[81]	Tilted angle focused ion beam milling process. (small area materials)	Slanted split ring nanoapertures milled in a single thick metal layer	1.56 at 760 nm,
[82]	Multistep lithography process (small area materials)	Sandwiched chiral meta-mirror consisting of an asymmetric-hole array perforated film, a thin dielectric layer, and an optically thick metallic back plane	0.5 at 880 nm
[50]	FIBID (small area materials)	Ensemble of helical nanowires comprising of Pt nanograins in an amorphous carbon matrix	~ 0.76
[83]	e-beam lithography, followed by gold deposition and lift-off (small area materials)	2D planar chiral metasurface consisting of a square array of unit cells comprising of asymmetric gold nanorods	~ 0.32
[84]	electron beam induced deposition (EBID) (small area materials)	Gold coated silica helices	0.86
[19]	FIB milling (small area materials)	Planar asymmetric L-shaped gold nanoantenna	~ 1.05 at ~ 1.45 μm

[85]	Laser direct write (small area materials)	Photonic helices from photoresist (65 µm by 65 µm footprint)	~ 1.55 at 4.3 µm
[12]	Laser direct write (small area materials)	3D gold helices	~1.68 at 4.7 µm
[58]	Laser interference lithography for periodic seed layer, e-beam evaporation based on GLAD for growth of silica helices, DC magnetron sputtering for TiN coating (large area materials)	Core silica helices coated by TiN	~ 0.34 at 600 nm
[56]	GLAD, e-beam evaporation (large area materials)	Metal decorated silica helical films	~ 0.3 at ~ 600 nm
[73]	GLAD, e-beam evaporation (large area materials)	Thermally annealed metal decorated silica helical films	~ 0.1 at ~ 610 nm
[4]	nanospherical-lens lithography (NLL) and hole–mask lithography (HML) (large area materials)	Large area twisted arc metamaterial	~ 0.315 at ~ 850 nm
This work	GLAD, e-beam evaporation (large area materials)	Metal decorated silica helical films	~ 1.6 at ~790 nm

Dissymmetry factor values were evaluated from printed transmission spectra.

In this study, we developed computational models and correlated their chiro-optical responses with that of experimental observations. The FEM unit cell, geometrical parameters of the helical template and the three models for left-handed configurations are shown in Fig. 3A-C. The experiments were carried out with air as the surrounding medium and we expect an overall red-shift [55] of the chiro-optical spectra for other media. Our initial attempt at developing a computational model incorporating the theoretical predictions and resembling the measured spectrum from the experimental system is Model I (Fig. 3C-I), which comprises of only spherical NPs. The scatter plot showing the radii (a) and center to center distances (r) of spherical particles is shown in Fig. 4A. The NPs are decorated on three arc lengths (*L1*, *L2*, *L3*) of the helical template so that the numerical model imitates an average helix on the actual sample which accommodates roughly 25 NPs on the complete helix; *L1* (11 NPs with radii a_1, a_2, … a_{11}), *L2* (5 NPs with radii a_1, a_3, a_4, a_5 and a_6) and *L3* (3 NPs with radii a_1, a_2 and a_4) consists of spherical NPs only. The radii of the NPs increase from bottom till apex of the helix as per scanning electron micrograph estimation and the NP particle radii a_1, a_2, …a_{11} are 25 nm, 30 nm, …75 nm respectively. There are other NPs which are mostly on the rod on which the silica helical template is grown which do not contribute to chirality. For computational simplicity, the silica helical template is neglected which contributes minimal CD response as established previously [56]. The dimensional parameters of the 2-turn helical template are pitch (p) = 270 nm, structure width (w) = 120 nm and wire thickness (d) = 100 nm. A histogram analysis from the computed r/a values of the developed computational model shown in Fig. 4B reveals that the particles are in tighter confinement (r/a<3) in close agreement with the experimental system and thus the analytical chiro-optical spectrum should contain information on the higher order multipolar effects. The existence of multipoles in the structure is evident from the maps of electric field and current density on AgNPs of Model II and III (shown in Fig. 3D) plotted at 610 nm and 612 nm respectively. Next, with Model II (shown in Fig. 3C-II), we intend to study the influence of the presence of a few ellipsoidal particles in the helix on the chiro-optical activity. This is done by replacing spherical NPs #1, 4, 7 and 11 in the arc length *L1* of Model I with ellipsoids of fixed axial ratio 1.5. Therefore Model II is predominantly consisting of spherical NPs with the presence of only four ellipsoidal NPs. We expect to note a redshift of the chiro-optical spectrum of Model II compared with that of Model I. Finally, the computational Model III in Fig. 3C-III largely consists of ellipsoids; arc lengths *L1* (11 NPs) and *L2* (5 NPs) consists of only ellipsoidal NPs while *L3* (3 NPs) consists of spherical NPs only. With Model III, we intend to study the effect of predominantly ellipsoidal NPs in the presence of very few spherical particles. Moreover, the samples considered in this study consist of unheated metal nanoparticles exhibiting random variations in sizes, spacings and orientations of particles which are attempted to be modelled with this numerical model. Therefore, Model III incorporates all random morphological variations in particles held in tighter confinement (r/a<3) beyond the coupled dipole approximation regime and thus the helix model closely resembles the experimental system.

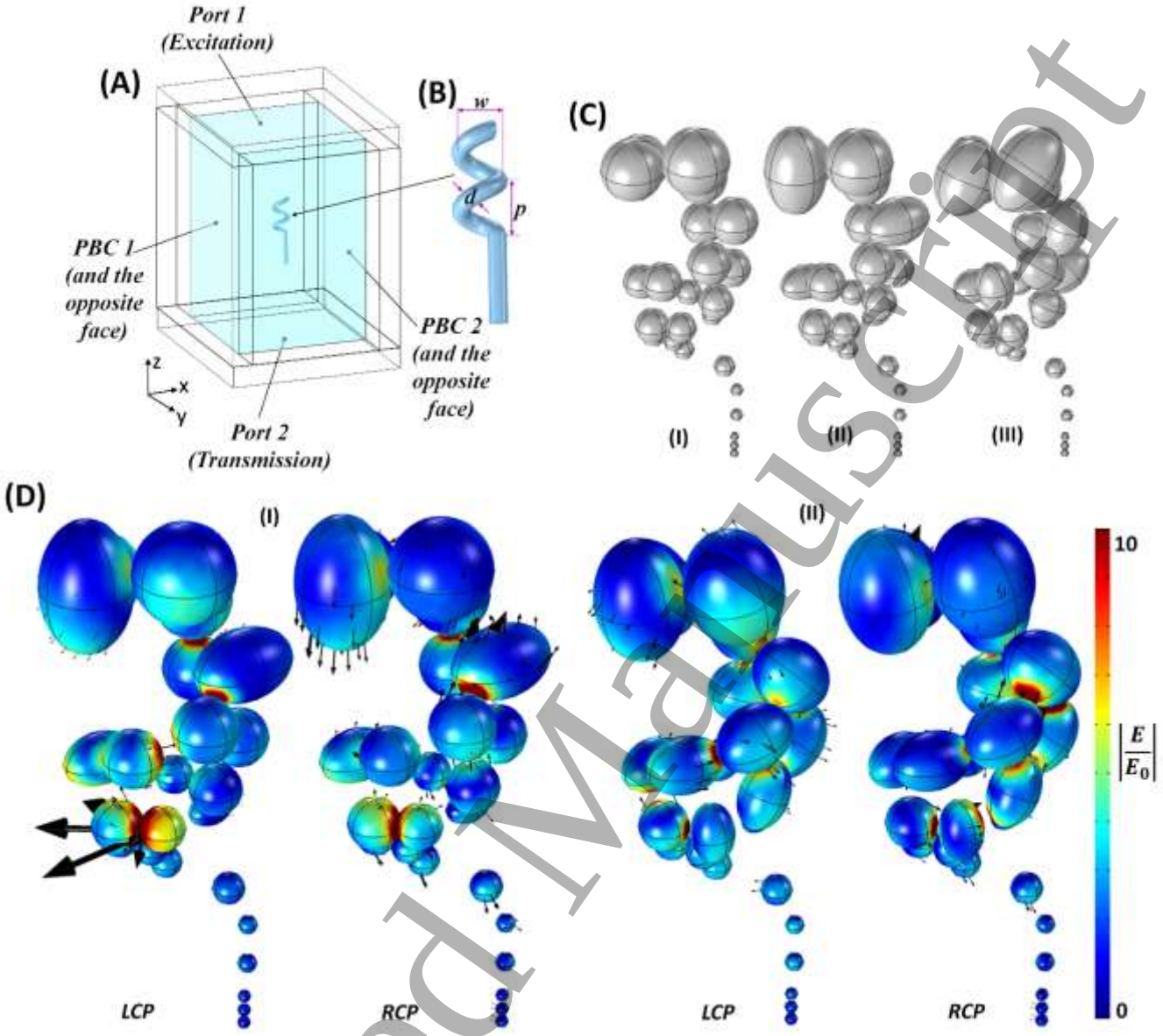

Figure 3. (A) FEM unit cell. For simulating the response of inter-helical nanostructures, periodic boundary conditions (PBC) are employed on the faces of the unit cell as shown. In the case when the response of a standalone single strand of helix is simulated, PBCs in x-y plane are replaced with perfectly matched layers (PMLs) as shown. (B) Geometrical parameters of the helical template of the nanostructure showing pitch (p), width (w) and thickness (d) of the silica helical template. (C) Three computational models of the nanoparticle distribution on the silica helical template for Plus 1 (Left-Handed sample) studied with helix simulation design parameters; turns = 2, w = 120 nm, p = 270 nm, and d = 100 nm. Model I: All spherical particles. Model II: Modified from Model I, consists of 4 ellipsoidal particles replaced by spherical particles. Model III: Largely consists of ellipsoidal particles of varying orientations and axial ratios. (D) Existence of multipoles in the structure is shown by maps of electric field and surface current density (shown by arrows) on (i) assembly of spherical and ellipsoidal NPs in Model II at $\lambda = 610$ nm and (ii) assembly of ellipsoidal NPs in one iteration case of Model III at $\lambda = 612$ nm. The length of the current arrow is proportional the current.

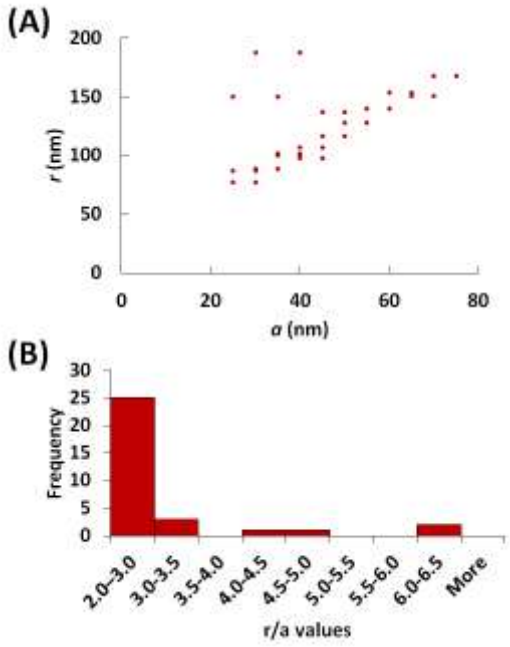

Figure 4. (A) Scatter plot of the center-to-center distances (r) and radii (a) of spherical particles of Model 1. (B) Histogram representing the weighted contribution of r/a values obtained from Model 1, showing most particles are at close separations (small r/a).

Figure 5 gives a comprehensive comparison of the simulation aspects correlated with the most important features of the experimental variability. Figure 5A shows numerically computed results of ΔT spectra for different lattice periodicities Λ = [470, 485, 500, 515, 530, 545, 560, 575, 590, 605] nm for Model I. The black curve shows a possible convolution (close to the experimental system) of ΔT spectra from the different lattice periodicities. We note that the different plasmonic modes (particularly the broad resonance noted at ~ 700 nm) of the system changes with increase in lattice periodicity in a redshifted manner as noted previously [86]–[88]. Further, for Λ > 530 nm, additional sharp plasmon peaks occur in the lower wavelength range which could be the result of a strong coupling mechanism between the higher order multipoles excited in the tightly confined particles which takes precedence over the lattice periodicity modes as Λ increases. It is noted from the convolution curve that ΔT values remain low up to wavelength range of 670 nm after which it increases up to 0.5 at ~ 700 nm and decreases further. Further, the amplitudes of ΔT spectra for Model I in periodic boundary condition when compared with that of a standalone single strand of helix in perfectly matched layer (PML) boundary condition (Fig. 5B) shows a similar trend in spectra, however the values for far-field ΔT are suppressed for PML case by a factor of approximately 3.6 at a noticeable resonance wavelength of ~ 690 nm. The suppressed numbers in far-field ΔT spectra in PML BC could possibly be explained by the absence of near-field interactions between adjacent helices which can significantly contribute to enhanced far-field ΔT response. Beyond Model I, we limit our numerical investigation to the study of NPs on a single strand of helix in PML BC for far-field calculations as opposed to helices considered in variable lattice periodicities which is close to the experimental system. This is because it is difficult to numerically model the large inconsistencies and non-uniformities in lattice periodicity of the helices. Moreover, the near-field effects in NPs of a single helix predominantly contributing towards the multipolar contributions, which is a major cause of the overall redshifted chiro-optical spectrum noted in the experimental system, can be effectively and conveniently modelled using a chiral arrangement of particles in a single strand of helix using PML BC.

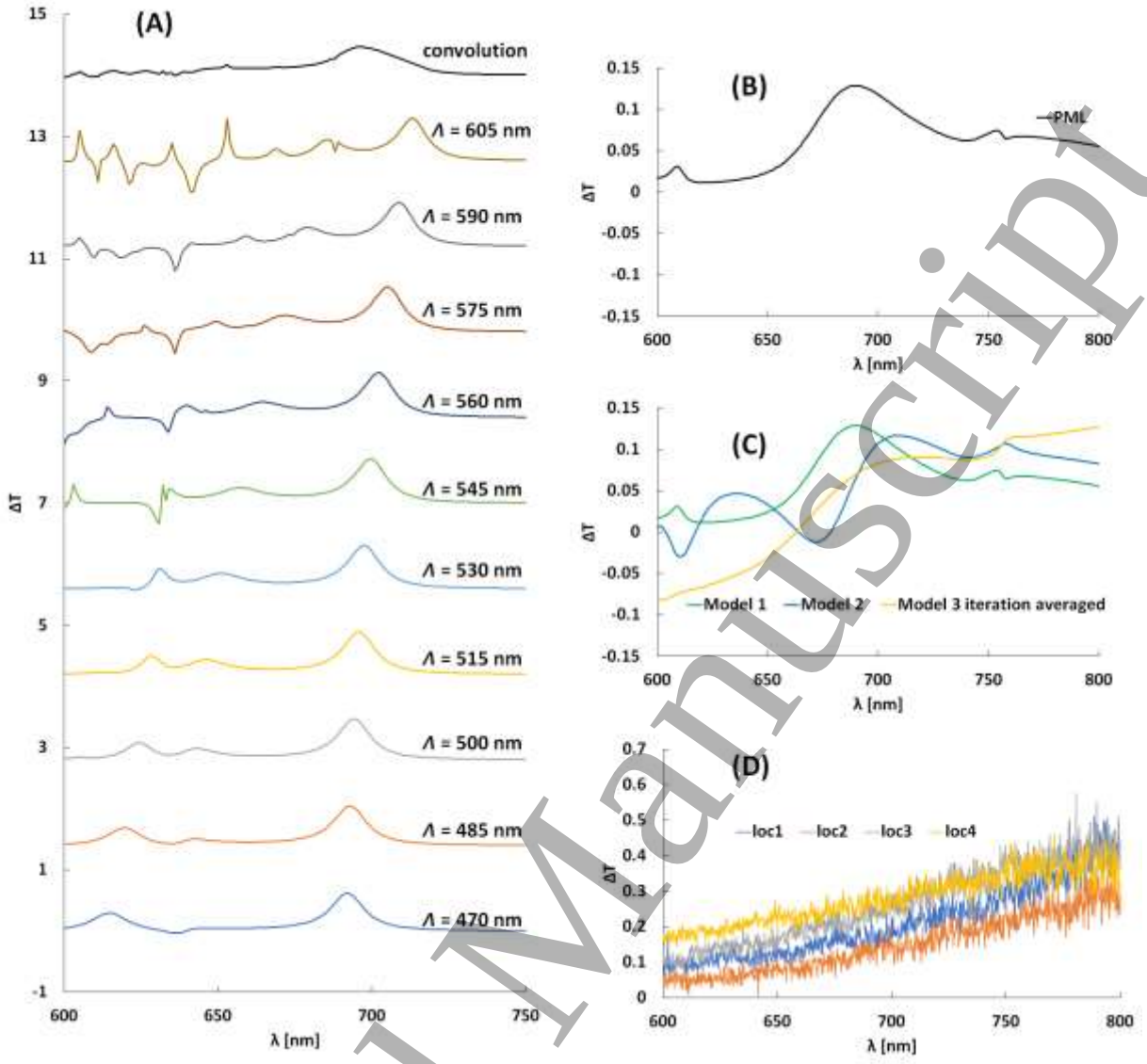

Figure 5. Comparison of simulated results with experimentally measured CD transmittance (A) FEM calculations for Model 1 for studying the effect of variation of periodicity of the lattice unit on ΔT. Each spectrum is vertically translated by 1.4. (B) FEM computed CD transmittance for the standalone single strand of helix of Model 1. (C) Comparison of ΔT for the three computational models for a standalone single strand of helix in PML boundary condition showing red-shifted spectra due to the presence of ellipsoidal particles as the model evolves from Model 1 to Model 3 (D) Measured CD transmittance for Plus 1 sample at four different locations on the sample.

Further, a direct comparison of this trend with the experimentally measured ΔT suggests that the values remain low for shorter wavelengths and increase for the longer wavelengths. The comparison of ΔT for the three computational models for a standalone single strand of helix in PML boundary is shown in Fig. 5C. To understand the increasing trend in the experimental ΔT spectra, we note ΔT spectra for Model II which significantly redshifts compared to Model I. The noted redshift could be explained as follows. In ellipsoidal NPs which are present in Model II, due to the anisotropic dimensionality, the resonances for oscillations will be different along major and minor axes of the ellipsoids. In a random arrangement of a large number of ellipsoids, the resonance along the major axis of ellipsoids is located at a longer wavelength [89]. Further, since the nanoparticle volume increases for ellipsoids compared to spherical NPs, a redshifted and a broadened plasmon band is noted as a result of stronger interparticle dipole–dipole interactions and larger absorption coefficient of the ellipsoids. This also explains the large differential transmittance response noted at higher wavelengths in both models due to the interaction of the

chirally arranged ellipsoids with the two contrasting states of the incident circularly polarized light.

We next consider Model III which largely consists of ellipsoidal particles and note that the ΔT spectrum is redshifted even further and the bisignate chiro-optical signature at ~ 700 nm becomes less evident and a visually broadened spectrum is noted. An analytical computational study has been done to generate 110 iteration models of Model III which consist of tightly confined NPs in $r/a<3$ regime and CD transmittance of the 110 iteration cases were numerically computed. For each iteration, the radius (b_i), randomly generated orientation (Θ_i) uniformly distributed in the range ($-\pi$, π) and randomly generated axial ratios (AR_i) uniformly distributed in the range (1.2, 1.5), the corresponding major (a_i) and minor (b_i) axes for all 16 ellipsoidal NPs in arc lengths *L1* and *L2* are obtained along with the computed center-center distance values (r_i); *i* is the NP index. While performing the random number generation of Θ_i and AR_i, also resulting in random values of a_i and b_i, the geometrical parameters of the helical template were fixed (p = 270 nm, w = 120 nm and d = 100 nm). Further, all 4 possible values of r/a between adjacent NPs, say NP(i) and NP(i+1), are calculated using the corresponding a_i and b_i values between the NPs (r_i/a_i; r_i/b_i). The iteration averaged plot of Model III in Fig. 5C is obtained from averaging the response from 110 FEM simulations. The sign of the chiroptical response is seen to change in ~ 600-670 nm which could occur because of changes in interference conditions between the incident optical excitation with the randomly oriented oscillating dipoles formed by AgNPs and the induced electric field of AgNPs due to the incident excitation which could be different from what is noted when $\lambda > 670$ nm. It is noted from the electric field distribution and current density (not shown here) through the assembly of AgNPs that there is a distinct surface redistribution of the energy of the multipoles excited in the helicoidal assembly of nanoparticles due to the incident excitation at lower wavelengths (612 nm and 640 nm) where the CD spectra exhibits a sign reversal. Further, a direct comparison of the measured and calculated values of absolute transmittance is shown in Fig. 6A from which it is noted that the measured and calculated spectra are in close agreement. Further, the spectra for both the measured and calculated circular differential transmittance, ΔT (shown in Figure 6B), distinctively follows an increasing trend towards the longer wavelengths. While the redshift trend is noted both experimentally and in simulations, the exact spectral features in simulations and experiments could not be matched possibly due to residual silver deposition or other complex variations in geometrical parameters in the experiment.

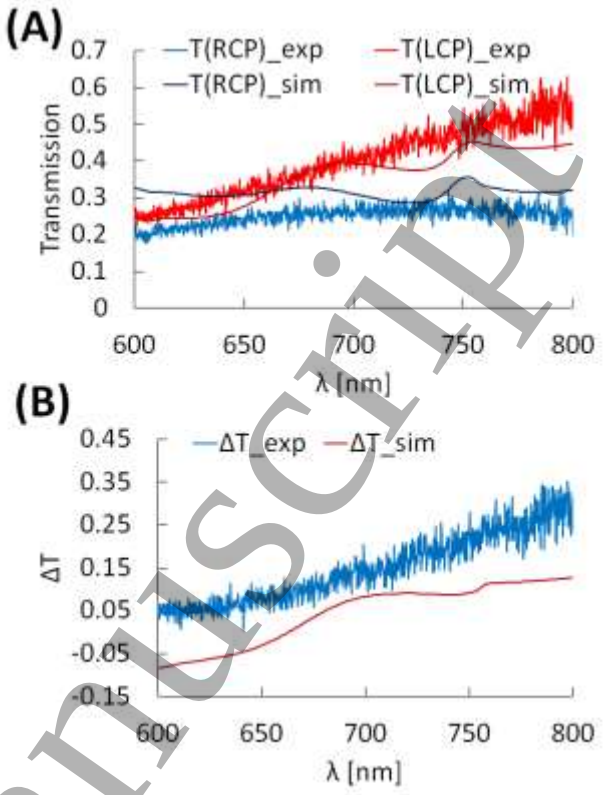

Figure 6. (A) Measured and calculated absolute transmittance. The calculated transmittance is obtained from one iteration case of Model III. (B) Measured and calculated circular differential transmittance (ΔT) response.

Next, a histogram representing the weighted contribution of the consolidated r/a values from the randomly generated helix with ellipsoidal NPs is shown in Fig. 7 from which it is noted that the r/a values for the iteration cases are indeed within the limit of the experimental system ($r/a<3$) and thus it is confirmed that our computational model indeed considers the predominant multipolar contributions which are present in the actual experimental system. Further, the presence of ellipsoidal NPs in the film has shown to push the spectra towards higher wavelengths at which enhanced chiro-optical signal is noted due to the strong near field interactions between the large number of randomly oriented dipoles and that of the twisted nature [6], [90], [91], of the incident electromagnetic field. Additionally, the occurrence of several multiple peaks in the CD transmittance response at shorter wavelengths could possibly be explained by the existence of different plasmonic modes in the system. The numerical simulations studying the influence of the variations of the structural parameters of the dielectric helical template, i.e., pitch and width are presented in Fig. S2. We numerically investigated the effect of the variation of pitch and width of the helical template of Model 2 in PML boundary condition on dissymmetry factor *g*. From the calculations on the effect of varying pitch with constant

width of 120 nm (Fig. S2(A)), it is found that the characteristic bisignate (dip-peak) nature of the chiro-optical signal at ~ 670 nm becomes evident for stretched helices with pitch more than 270 nm which is in agreement with the theoretical calculations established previously [92]. Further, from the calculations on width variation of the helical template with constant pitch of 270 nm (Fig. S2(B)), it is noted that the bisignate nature of the chiro-optical signal becomes less dramatic as the width increases which could possibly be explained by the weakened NP-NP interaction in the helical strand, thus reducing the effect of the characteristic bisignate nature of the chiro-optical signal.

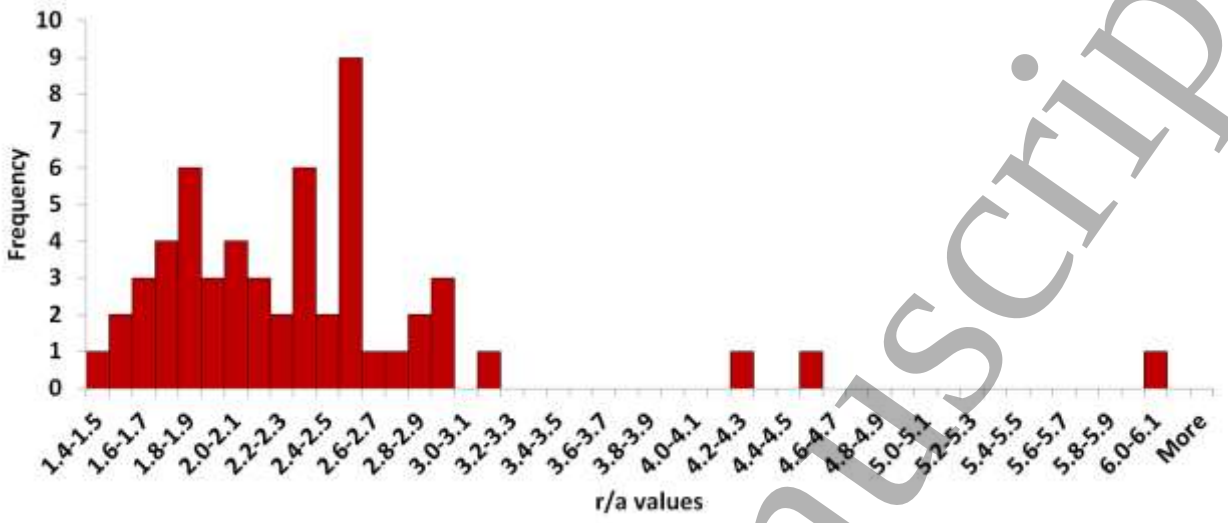

Figure 7. Histogram representing the weighted contribution of *r*/*a* values obtained from an average helix on the sample for an iteration case of Model 3 for randomly generated Θ_i and AR_i of the ellipsoids on the helix.

Figure 8(A) show transmission spectra for the helix of Model 3 under LCP and RCP excitation. We note a dissymmetry in transmission distinctively at λ = 691 nm and λ = 758 nm which is revealed from *g*-spectrum, where the maximum values of *g* at the two wavelengths are 0.3 and 0.35, respectively. Figure 8(B) shows maps of normalized optical chirality density or enhancements of the local optical chirality in the helix under LCP or RCP excitation, given by $\hat{C}_{L(R)} = \frac{C}{C_{CPL}}$, where the electromagnetic chirality density, *C* is defined as [93], [94]

$$C = -\frac{\epsilon_0 \omega}{2} Im(\boldsymbol{E}^*.\boldsymbol{B}) \qquad (2)$$

where $\boldsymbol{E}$ and $\boldsymbol{B}$ represent complex field quantities, ϵ_0 is permittivity of free space and ω is angular frequency of light. C_{CPL} represents optical chirality of the field in free space, given by $C_{CPL} = \pm\frac{\epsilon_0 \omega}{2c}\boldsymbol{E}_0{}^2$, where $\boldsymbol{E}_0$ is the incident electric field magnitude. The asymmetric redistribution of the chiral electromagnetic hotspots noted in the helical structure with ellipsoidal NPs due to the largely anisotropic nature of the plasmonic structure causes the large values of dissymmetry factor and thus resulting in enhanced chiro-optical activity. The theoretical limit of *g* is ±2. It is interesting to note that the experimentally realized values of *g* (see Fig. 2C, D) are as large as ~1.6, which is the largest reported for wafer scalable chiro-plasmonic samples till now. Further, when compared with the calculated dissymmetry factors for the helical structure of Model 1 (only spherical NPs), where although the enhanced chiro-optical spectra are comparatively blue-shifted, the calculated *g* values are also substantially high, even close to the theoretical limit. This further confirms that the predictions of chiro-optical response from the numerical simulations of the developed computational models are in close agreement with that realized experimentally. It is interesting to note that the spectral feature at 758 nm has an asymmetric profile. This asymmetric Fano line-shape could occur because of plasmon hybridization between the higher order multipoles excited in the ellipsoidal NPs when multiple ellipsoids in the overall assembly of NPs could align almost parallelly. The overlap and interference between the higher order multipoles excited along the long axis of the ellipsoidal NPs could result in the asymmetric line-shape. Also, it is noted that the resonance is not quite sharp which could possibly be due to a rather weak coupling mechanism which could occur between ellipsoids of disproportionate lengths in the extrinsically chiral assembly [95], [96].The information from the computational predictions and its concurrence with the experimental data is highly relevant for enantiomer selective identification and sensing applications since the wafer scalable nanostructured films considered in this study are inherently porous easily allowing the diffusion of chiral molecules in regions of enhanced chiral electromagnetic hotspots.

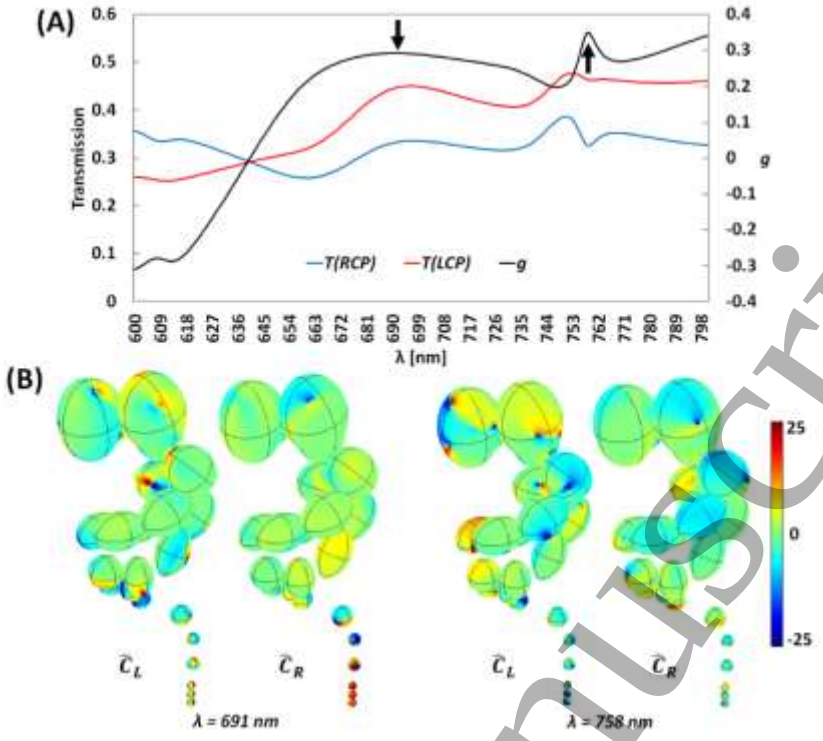

Figure 8. (A) Calculated transmission spectra of helix of Model 3 under LCP and RCP excitation and dissymmetry factor *g*. (B) Maps of local optical chirality enhancements on the helix under LCP and RCP excitation at λ = 691 nm and λ = 758 nm.

4. Conclusions

In summary with a computational model resembling the material system, we have numerically investigated and correlated the large experimental chiro-optical response from a wafer scale nanostructured film of ellipsoidal AgNPs on unseeded aperiodic dielectric silica helices. While the previous computational models in literature have studied variations of individual design parameters, the chosen computational model of an intrinsically chiral dielectric helix with ellipsoidal particles considers almost all variabilities in terms of morphologies of particles, silica helical template and aperiodic helices due to unseeded substrate. We investigated the chiro-optical response of chirally arranged ellipsoidal AgNPs in tighter confinement (r/a<3) and thus our computationally evaluated findings of the large chiro-optical response incorporating the predominant multipolar contributions of the plasmonic interactions conform well with the measured material system. Our findings on the computational investigations and their close correlation with the experimental observations on the large chiro-optical response of the highly wafer-scalable films incorporating a simple fabrication technique contribute to the understanding of complex multipolar response in chiral light-matter interactions.

Acknowledgements

AN thanks IIT Delhi and acknowledges Overseas Visiting Doctoral Fellowship from the Science and Engineering Research Board (SERB) of India. AG, PS, ZX acknowledge funding support from MHRD, MeitY and DST Nano Mission through NNetRA. XX wishes to thank the support from the US National Science Foundation (CBET-1804377).

References

[1] Pendry, J.B., 2004. A chiral route to negative refraction. *Science*, ***306***(5700), pp.1353-1355.

[2] Zhang, S., Park, Y.S., Li, J., Lu, X., Zhang, W. and Zhang, X., 2009. Negative refractive index in chiral metamaterials. *Physical review letters*, ***102***(2), p.023901.

[3] Tullius, R., Platt, G.W., Khosravi Khorashad, L., Gadegaard, N., Lapthorn, A.J., Rotello, V.M., Cooke, G., Barron, L.D., Govorov, A.O., Karimullah, A.S. and Kadodwala, M., 2017. Superchiral plasmonic phase sensitivity for fingerprinting of protein interface structure. *ACS nano*, ***11***(12), pp.12049-12056.

[4] Lin, C.Y., Liu, C.C., Chen, Y.Y., Chiu, K.Y., Wu, J.D., Lin, B.L., Wang, C.H., Chen, Y.F., Chang, S.H. and Chang, Y.C., 2020. Molecular Chirality Detection with Periodic Arrays of Three-Dimensional Twisted Metamaterials. *ACS Applied Materials & Interfaces*. ***13(***1), pp. 1152–1157

[5] Han, B., Gao, X., Lv, J. and Tang, Z., 2020. Magnetic circular dichroism in nanomaterials: New opportunity in understanding and modulation of excitonic and plasmonic resonances. *Advanced Materials*, ***32***(41), p.1801491.

[6] Hendry, E., Carpy, T., Johnston, J., Popland, M., Mikhaylovskiy, R.V., Lapthorn, A.J., Kelly, S.M., Barron, L.D., Gadegaard, N. and Kadodwala, M.J.N.N., 2010. Ultrasensitive detection and characterization of biomolecules using superchiral fields. *Nature nanotechnology*, ***5***(11), pp.783-787.

[7] Tullius, R., Karimullah, A.S., Rodier, M., Fitzpatrick, B., Gadegaard, N., Barron, L.D., Rotello, V.M., Cooke, G., Lapthorn, A. and Kadodwala, M., 2015. "Superchiral" spectroscopy: detection of protein higher order hierarchical structure with chiral plasmonic nanostructures. *Journal of the American Chemical Society*, ***137***(26), pp.8380-8383.

[8] Khoo, E.H., Leong, E.S., Wu, S.J., Phua, W.K., Hor, Y.L. and Liu, Y.J., 2016. Effects of asymmetric nanostructures on the extinction difference properties of actin biomolecules and filaments. *Scientific reports*, ***6***(1), pp.1-11.

[9] Jack, C., Karimullah, A.S., Leyman, R., Tullius, R., Rotello, V.M., Cooke, G., Gadegaard, N., Barron, L.D. and Kadodwala, M., 2016. Biomacromolecular stereostructure mediates mode hybridization in chiral plasmonic nanostructures. *Nano letters*, ***16***(9), pp.5806-5814.

[10] García-Guirado, J., Svedendahl, M., Puigdollers, J. and Quidant, R., 2018. Enantiomer-selective molecular sensing using racemic nanoplasmonic arrays. *Nano letters*, ***18***(10), pp.6279-6285.

[11] Zhao, Y., Askarpour, A.N., Sun, L., Shi, J., Li, X. and Alù, A., 2017. Chirality detection of enantiomers using twisted optical metamaterials. *Nature communications*, ***8***(1), pp.1-8.

[12] Gansel, J.K., Thiel, M., Rill, M.S., Decker, M., Bade, K., Saile, V., von Freymann, G., Linden, S. and Wegener, M., 2009. Gold helix photonic metamaterial as broadband circular polarizer. *Science*, ***325***(5947), pp.1513-1515.

[13] Zhao, Y., Belkin, M.A. and Alù, A., 2012. Twisted optical metamaterials for planarized ultrathin broadband circular polarizers. *Nature communications*, ***3***(1), pp.1-7.

[14] Choi, W.J., Cheng, G., Huang, Z., Zhang, S., Norris, T.B. and Kotov, N.A., 2019. Terahertz circular dichroism spectroscopy of biomaterials enabled by kirigami polarization modulators. *Nature materials*, ***18***(8), pp.820-826.

[15] Verre, R., Shao, L., Odebo Länk, N., Karpinski, P., Yankovich, A.B., Antosiewicz, T.J., Olsson, E. and Käll, M., 2017. Metasurfaces and colloidal suspensions composed of 3D chiral Si nanoresonators. *Advanced Materials*, ***29***(29), p.1701352.

[16] Patti, F., Saija, R., Denti, P., Pellegrini, G., Biagioni, P., Iatì, M.A. and Maragò, O.M., 2019. Chiral optical tweezers for optically active particles in the T-matrix formalism. *Scientific reports*, ***9***(1), pp.1-10.

[17] Yeom, J., Guimaraes, P.P., Ahn, H.M., Jung, B.K., Hu, Q., McHugh, K., Mitchell, M.J., Yun, C.O., Langer, R. and Jaklenec, A., 2020. Chiral supraparticles for controllable nanomedicine. *Advanced Materials*, ***32***(1), p.1903878.

[18] Collins, J.T., Kuppe, C., Hooper, D.C., Sibilia, C., Centini, M. and Valev, V.K., 2017. Chirality and chiroptical effects in metal nanostructures: fundamentals and current trends. *Advanced Optical Materials*, ***5***(16), p.1700182.

[19] Ye, W., Yuan, X., Guo, C., Zhang, J., Yang, B. and Zhang, S., 2017. Large chiroptical effects in planar chiral metamaterials. *Physical Review Applied*, ***7***(5), p.054003.

[20] Chen, C., Gao, S., Song, W., Li, H., Zhu, S.N. and Li, T., 2021. Metasurfaces with Planar Chiral Meta-Atoms for Spin Light Manipulation. *Nano Letters*, ***21***, pp. 1815–1821.

[21] Ni, J., Liu, S., Hu, G., Hu, Y., Lao, Z., Li, J., Zhang, Q., Wu, D., Dong, S., Chu, J. and Qiu, C.W., 2021. Giant Helical Dichroism of Single Chiral Nanostructures with Photonic Orbital Angular Momentum. *ACS nano*, ***15***, pp. 2893–2900.

[22] Yeom, J., Santos, U.S., Chekini, M., Cha, M., de Moura, A.F. and Kotov, N.A., 2018. Chiromagnetic nanoparticles and gels. *Science*, ***359***(6373), pp.309-314.

[23] Zhao, Y., Saleh, A.A., Van De Haar, M.A., Baum, B., Briggs, J.A., Lay, A., Reyes-Becerra, O.A. and Dionne, J.A., 2017. Nanoscopic control and quantification of enantioselective optical forces. *Nature nanotechnology*, ***12***(11), p.1055.

[24] Kong, X.T., Khosravi Khorashad, L., Wang, Z. and Govorov, A.O., 2018. Photothermal circular dichroism induced by plasmon resonances in chiral metamaterial absorbers and bolometers. *Nano letters*, ***18***(3), pp.2001-2008.

[25] Cho, N.H., Byun, G.H., Lim, Y.C., Im, S.W., Kim, H., Lee, H.E., Ahn, H.Y. and Nam, K.T., 2020. Uniform chiral gap synthesis for high dissymmetry factor in single plasmonic gold nanoparticle. *ACS nano*, ***14***(3), pp.3595-3602.

[26] Jung, A., Kim, C. and Yeom, B., 2017. Birefringence-Induced Modulation of Optical Activity in Chiral Plasmonic Helical Arrays. *The journal of physical chemistry letters*, ***8***(8), pp.1872-1877.

[27] Jeong, K.J., Lee, D.K., Tran, V.T., Wang, C., Lv, J., Park, J., Tang, Z. and Lee, J., 2020. Helical Magnetic Field-Induced Real-Time Plasmonic Chirality Modulation. *ACS nano*, ***14***(6), pp.7152-7160.

[28] Wen, H., Song, S., Xie, F., Wang, B., Xu, J., Feng, Z., Wu, S., Han, J., Guan, B.O., Xu, X. and Cao, Y., 2020. Great chiral fluorescence from the optical duality of silver nanostructures enabled by 3D laser printing. *Materials Horizons*, ***7***(12), pp.3201-3208.

[29] Vestler, D., Shishkin, I., Gurvitz, E.A., Nasir, M.E., Ben-Moshe, A., Slobozhanyuk, A.P., Krasavin, A.V., Levi-Belenkova, T., Shalin, A.S., Ginzburg, P. and Markovich, G., 2018. Circular dichroism enhancement in plasmonic nanorod metamaterials. *Optics express*, ***26***(14), pp.17841-17848.

[30] Tang, C., Chen, F., Du, J. and Hou, Y., 2020. Large-area cavity-enhanced 3D chiral metamaterials based on the angle-dependent deposition technique. *Nanoscale*, ***12***(16), pp.9162-9170.

[31] Lee, Y.Y., Kim, R.M., Im, S.W., Balamurugan, M. and Nam, K.T., 2020. Plasmonic metamaterials for chiral sensing applications. *Nanoscale*, ***12***(1), pp.58-66.

[32] Frenzel, T., Hahn, V., Ziemke, P., Schneider, J.L.G., Chen, Y., Kiefer, P., Gumbsch, P. and Wegener, M., 2021. Large characteristic lengths in 3D chiral elastic metamaterials. *Communications Materials*, ***2***(1), pp.1-9.

[33] Wu, W., Hu, W., Qian, G., Liao, H., Xu, X. and Berto, F., 2019. Mechanical design and multifunctional applications of chiral mechanical metamaterials: A review. *Materials & Design*, ***180***, p.107950.

[34] Hentschel, M., Schäferling, M., Duan, X., Giessen, H. and Liu, N., 2017. Chiral plasmonics. *Science advances*, ***3***(5), p.e1602735.

[35] Hwang, M. and Yeom, B., 2020. Fabrication of Chiral Materials in Nano-and Microscale. *Chemistry of Materials*. **33**, pp. 807–817.

[36] Park, H.S., Kim, T.T., Kim, H.D., Kim, K. and Min, B., 2014. Nondispersive optical activity of meshed helical metamaterials. *Nature communications*, ***5***(1), pp.1-7.

[37] Cui, Y., Kang, L., Lan, S., Rodrigues, S. and Cai, W., 2014. Giant chiral optical response from a twisted-arc metamaterial. *Nano letters*, ***14***(2), pp.1021-1025.

[38] Fang, Y., Verre, R., Shao, L., Nordlander, P. and Käll, M., 2016. Hot electron generation and cathodoluminescence nanoscopy of chiral split ring resonators. *Nano letters*, ***16***(8), pp.5183-5190.

[39] Kuzyk, A., Schreiber, R., Fan, Z., Pardatscher, G., Roller, E.M., Högele, A., Simmel, F.C., Govorov, A.O. and Liedl, T., 2012. DNA-based self-assembly of chiral plasmonic nanostructures with tailored optical response. *Nature*, ***483***(7389), pp.311-314.

[40] Lan, X., Lu, X., Shen, C., Ke, Y., Ni, W. and Wang, Q., 2015. Au nanorod helical superstructures with designed chirality. *Journal of the American Chemical Society*, ***137***(1), pp.457-462.

[41] Schreiber, R., Luong, N., Fan, Z., Kuzyk, A., Nickels, P.C., Zhang, T., Smith, D.M., Yurke, B., Kuang, W., Govorov, A.O. and Liedl, T., 2013. Chiral plasmonic DNA nanostructures with switchable circular dichroism. *Nature communications*, ***4***(1), pp.1-6.

[42] Urban, M.J., Dutta, P.K., Wang, P., Duan, X., Shen, X., Ding, B., Ke, Y. and Liu, N., 2016. Plasmonic toroidal metamolecules assembled by DNA origami. *Journal of the American Chemical Society*, ***138***(17), pp.5495-5498.

[43] Han, B., Zhu, Z., Li, Z., Zhang, W. and Tang, Z., 2014. Conformation modulated optical activity enhancement in chiral cysteine and Au nanorod assemblies. *Journal of the American Chemical Society*, ***136***(46), pp.16104-16107.

[44] Wang, R.Y., Wang, H., Wu, X., Ji, Y., Wang, P., Qu, Y. and Chung, T.S., 2011. Chiral assembly of gold nanorods with collective plasmonic circular dichroism response. *Soft Matter*, ***7***(18), pp.8370-8375.

[45] Querejeta-Fernández, A., Chauve, G., Methot, M., Bouchard, J. and Kumacheva, E., 2014. Chiral plasmonic films formed by gold nanorods and cellulose nanocrystals. *Journal of the American Chemical Society*, ***136***(12), pp.4788-4793.

[46] Han, C., Leung, H.M., Chan, C.T. and Tam, W.Y., 2015. Giant plasmonic circular dichroism in Ag staircase nanostructures. *Optics express*, ***23***(26), pp.33065-33078.

[47] Dietrich, K., Menzel, C., Lehr, D., Puffky, O., Hübner, U., Pertsch, T., Tünnermann, A. and Kley, E.B., 2014. Elevating optical activity: Efficient on-edge lithography of three-dimensional starfish metamaterial. *Applied Physics Letters*, ***104***(19), p.193107.

[48] Yeom, B., Zhang, H., Zhang, H., Park, J.I., Kim, K., Govorov, A.O. and Kotov, N.A., 2013. Chiral plasmonic nanostructures on achiral nanopillars. *Nano letters*, ***13***(11), pp.5277-5283.

[49] Radke, A., Gissibl, T., Klotzbücher, T., Braun, P.V. and Giessen, H., 2011. Three-dimensional bichiral plasmonic crystals fabricated by direct laser writing and electroless silver plating. *Advanced Materials*, ***23***(27), pp.3018-3021.

[50] Esposito, M., Tasco, V., Todisco, F., Cuscunà, M., Benedetti, A., Scuderi, M., Nicotra, G. and Passaseo, A., 2016. Programmable extreme chirality in the visible by helix-shaped metamaterial platform. *Nano letters*, ***16***(9), pp.5823-5828.

[51] Wu, Z., Chen, X., Wang, M., Dong, J. and Zheng, Y., 2018. High-performance ultrathin active chiral metamaterials. *ACS nano*, ***12***(5), pp.5030-5041.

[52] Dietrich, K., Lehr, D., Helgert, C., Tünnermann, A. and Kley, E.B., 2012. Circular Dichroism from Chiral Nanomaterial Fabricated by On-Edge Lithography. *Advanced Materials*, ***24***(44), pp.OP321-OP325.

[53] Steele, J.J. and Brett, M.J., 2007. Nanostructure engineering in porous columnar thin films: recent advances. *Journal of Materials Science: Materials in Electronics*, ***18***(4), pp.367-379.

[54] Hawkeye, M.M. and Brett, M.J., 2007. Glancing angle deposition: Fabrication, properties, and applications of micro-and nanostructured thin films. *Journal of Vacuum Science & Technology A: Vacuum, Surfaces, and Films*, ***25***(5), pp.1317-1335.

[55] Nair, G., Singh, H.J. and Ghosh, A., 2015. Tuning the chiro-plasmonic response using high refractive index-dielectric templates. *Journal of Materials Chemistry C*, ***3***(26), pp.6831-6835.

[56] Singh, J.H., Nair, G., Ghosh, A. and Ghosh, A., 2013. Wafer scale fabrication of porous three-dimensional plasmonic metamaterials for the visible region: chiral and beyond. *Nanoscale*, ***5***(16), pp.7224-7228.

[57] Mark, A.G., Gibbs, J.G., Lee, T.C. and Fischer, P., 2013. Hybrid nanocolloids with programmed three-dimensional shape and material composition. *Nature materials*, ***12***(9), pp.802-807.

[58] Venkataramanababu, S., Nair, G., Deshpande, P., Jithin, M.A., Mohan, S. and Ghosh, A., 2018. Chiro-plasmonic refractory metamaterial with titanium nitride (TiN) core–shell nanohelices. *Nanotechnology*, ***29***(25), p.255203.

[59] Singh, H.J. and Ghosh, A., 2018. Large and tunable chiro-optical response with all dielectric helical nanomaterials. *ACS Photonics*, ***5***(5), pp.1977-1985.

[60] Singh, H.J. and Ghosh, A., 2018. Chiral assemblies of achiral dielectric nanoparticles: semianalytical approach. *The Journal of Physical Chemistry C*, ***122***(35), pp.20476-20482.

[61] Singh, H.J. and Ghosh, A., 2018. Harnessing magnetic dipole resonance in novel dielectric nanomaterials. *Nanoscale*, ***10***(34), pp.16102-16106.

[62] Singh, H.J. and Ghosh, A., 2014, December. Variability on the chiro-optical response of helically arranged metallic nanoparticles. In *2014 IEEE 2nd International Conference on Emerging Electronics (ICEE)* (pp. 1-4). IEEE.

[63] Fan, Z. and Govorov, A.O., 2010. Plasmonic circular dichroism of chiral metal nanoparticle assemblies. *Nano letters*, ***10***(7), pp.2580-2587.

[64] Draine, B.T. and Flatau, P.J., 1994. Discrete-dipole approximation for scattering calculations. *Josa a*, ***11***(4), pp.1491-1499.

[65] Markel, V.A., 1993. Coupled-dipole approach to scattering of light from a one-dimensional periodic dipole structure. *Journal of Modern Optics*, ***40***(11), pp.2281-2291.

[66] Zhao, L., Kelly, K.L. and Schatz, G.C., 2003. The extinction spectra of silver nanoparticle arrays: influence of array structure on plasmon resonance wavelength and width. *The Journal of Physical Chemistry B*, ***107***(30), pp.7343-7350.

[67] Zou, S. and Schatz, G.C., 2004. Narrow plasmonic/photonic extinction and scattering line shapes for one and two dimensional silver nanoparticle arrays. *The Journal of chemical physics*, ***121***(24), pp.12606-12612.

[68] Park, S.Y. and Stroud, D., 2004. Surface-plasmon dispersion relations in chains of metallic nanoparticles: An exact quasistatic calculation. *Physical Review B*, ***69***(12), p.125418.

[69] Weber, W.H. and Ford, G.W., 2004. Propagation of optical excitations by dipolar interactions in metal nanoparticle chains. *Physical Review B*, ***70***(12), p.125429.

[70] Nordlander, P., Oubre, C., Prodan, E., Li, K. and Stockman, M.I., 2004. Plasmon hybridization in nanoparticle dimers. *Nano letters*, ***4***(5), pp.899-903.

[71] Gunnarsson, L., Rindzevicius, T., Prikulis, J., Kasemo, B., Käll, M., Zou, S. and Schatz, G.C., 2005. Confined plasmons in nanofabricated single silver particle pairs: experimental observations of strong interparticle interactions. *The Journal of Physical Chemistry B*, ***109***(3), pp.1079-1087.

[72] Jain, P.K., Huang, W. and El-Sayed, M.A., 2007. On the universal scaling behavior of the distance decay of plasmon coupling in metal nanoparticle pairs: a plasmon ruler equation. *Nano Letters*, ***7***(7), pp.2080-2088.

[73] Nair, G., Singh, H.J., Paria, D., Venkatapathi, M. and Ghosh, A., 2014. Plasmonic interactions at close proximity in chiral geometries: route toward broadband chiroptical response and giant enantiomeric sensitivity. *The Journal of Physical Chemistry C*, ***118***(9), pp.4991-4997.

[74] Johnson, P.B. and Christy, R.W., 1972. Optical constants of the noble metals. *Physical review B*, ***6***(12), p.4370.

[75] Araújo, A., Mendes, M.J., Mateus, T., Vicente, A., Nunes, D., Calmeiro, T., Fortunato, E., Águas, H. and Martins, R., 2016. Influence of the substrate on the morphology of self-assembled silver nanoparticles by rapid thermal annealing. *The Journal of Physical Chemistry C*, ***120***(32), pp.18235-18242.

[76] Abbas, N., Shad, M.R., Hussain, M., Mehdi, S.M.Z. and Sajjad, U., 2019. Fabrication and characterization of silver thin films using physical vapor deposition, and the investigation of annealing effects on their structures. *Materials Research Express*, ***6***(11), p.116437.

[77] Taschuk, M. T., Hawkeye, M. M., and Brett, M. J., 2010. *Glancing Angle Deposition. Chapter in Handbook of Deposition Technologies for Films and Coatings: Science, Applications and Technology*, 3rd ed. Oxford, United Kingdom: Elsevier.

[78] Suri, P., Deshpande, P. and Ghosh, A., 2018, December. Selective dewetting of metal films for fabrication of atomically separated nanoplasmonic dimers. In *2018 4th IEEE International Conference on Emerging Electronics (ICEE)* (pp. 1-4). IEEE.

[79] Höflich, K., Feichtner, T., Hansjürgen, E., Haverkamp, C., Kollmann, H., Lienau, C. and Silies, M., 2019. Resonant behavior of a single plasmonic helix. *Optica*, ***6***(9), pp.1098-1105.

[80] Rajaei, M., Zeng, J., Albooyeh, M., Kamandi, M., Hanifeh, M., Capolino, F. and Wickramasinghe, H.K., 2019. Giant circular dichroism at visible frequencies enabled by plasmonic ramp-shaped nanostructures. *ACS Photonics*, ***6***(4), pp.924-931.

[81] Chen, Y., Gao, J. and Yang, X., 2018. Chiral metamaterials of plasmonic slanted nanoapertures with symmetry breaking. *Nano letters*, ***18***(1), pp.520-527.

[82] Kang, L., Rodrigues, S.P., Taghinejad, M., Lan, S., Lee, K.T., Liu, Y., Werner, D.H., Urbas, A. and Cai, W., 2017. Preserving spin states upon reflection: linear and nonlinear responses of a chiral meta-mirror. *Nano letters*, ***17***(11), pp.7102-7109.

[83] Khanikaev, A.B., Arju, N., Fan, Z., Purtseladze, D., Lu, F., Lee, J., Sarriugarte, P., Schnell, M., Hillenbrand, R., Belkin, M.A. and Shvets, G., 2016. Experimental demonstration of the microscopic origin of circular dichroism in two-dimensional metamaterials. *Nature communications*, ***7***(1), pp.1-8.

[84] Kosters, D., De Hoogh, A., Zeijlemaker, H., Acar, H., Rotenberg, N. and Kuipers, L., 2017. Core–shell plasmonic nanohelices. *ACS photonics*, ***4***(7), pp.1858-1863.

[85] Thiel, M., Fischer, H., Von Freymann, G. and Wegener, M., 2010. Three-dimensional chiral photonic superlattices. *Optics letters*, ***35***(2), pp.166-168.

[86] Barnes, W.L., Dereux, A. and Ebbesen, T.W., 2003. Surface plasmon subwavelength optics. *nature*, ***424***(6950), pp.824-830.

[87] Gupta, N. and Dhawan, A., 2018. Bridged-bowtie and cross bridged-bowtie nanohole arrays as SERS substrates with hotspot tunability and multi-wavelength SERS response. *Optics express*, ***26***(14), pp.17899-17915.

[88] Ninawe, A., Dhawan, A. and Xu, X., 2020. Numerical investigation of a narrowband absorber with a simple structure. *OSA Continuum*, ***3***(12), pp.3582-3594.

[89] Liz-Marzán, L.M., 2006. Tailoring surface plasmons through the morphology and assembly of metal nanoparticles. *Langmuir*, ***22***(1), pp.32-41.

[90] Tang, Y. and Cohen, A.E., 2011. Enhanced enantioselectivity in excitation of chiral molecules by superchiral light. *Science*, ***332***(6027), pp.333-336.

[91] Davis, T.J. and Hendry, E., 2013. Superchiral electromagnetic fields created by surface plasmons in nonchiral metallic nanostructures. *Physical Review B*, ***87***(8), p.085405.

[92] Fan, Z. and Govorov, A.O., 2011. Helical metal nanoparticle assemblies with defects: plasmonic chirality and circular dichroism. *The Journal of Physical Chemistry C*, ***115***(27), pp.13254-13261.

[93] García-Etxarri, A. and Dionne, J.A., 2013. Surface-enhanced circular dichroism spectroscopy mediated by nonchiral nanoantennas. *Physical Review B*, ***87***(23), p.235409.

[94] Lipkin, D.M., 1964. Existence of a new conservation law in electromagnetic theory. *Journal of Mathematical Physics*, ***5***(5), pp.696-700.

[95] Tian, X., Fang, Y. and Zhang, B., 2014. Multipolar Fano resonances and Fano-assisted optical activity in silver nanorice heterodimers. *Acs Photonics*, ***1***(11), pp.1156-1164.

[96] Hu, L., Huang, Y., Fang, L., Chen, G., Wei, H. and Fang, Y., 2015. Fano resonance assisting plasmonic circular dichroism from nanorice heterodimers for extrinsic chirality. *Scientific reports*, ***5***(1), pp.1-9.